Chemical Science

ROYAL SOCIETY OF CHEMISTRY

EDGE ARTICLE

View Article Online
View Journal

Cite this: DOI: 10.1039/d5sc09651k

All publication charges for this article have been paid for by the Royal Society of Chemistry

Deciphering the stimuli-responsive behavior of TPPE-incorporated flexible metal–organic frameworks

You Fan,[ac] Zhikai Zhu,[c] Shuo Zhou,[c] Federico Gorelli,[c] Yuchen Ye,[c] Huixin Hu,[c] Shenghan Zhang,[c] Hongliang Dong,[c] Changzhong Liao, *[a] Ziyou Zhang *[bc] and Zhiqiang Chen *[c]

Received 9th December 2025
Accepted 5th April 2026

DOI: 10.1039/d5sc09651k

rsc.li/chemical-science

Aggregation-induced emission luminogens (AIEgens) hold great promise for the design of highly sensitive and stimulus-responsive luminescent metal–organic frameworks (LMOFs). However, the underlying response mechanisms, particularly the evolution of the energy state and conformation of AIE linkers under external stimuli, remain insufficiently understood. Here, we investigate a three-dimensional MOF, $[Cd_2(D\text{-}Cam)_2(TPPE)]_n$ (D-MOF), and demonstrate that conformational locking of the flexible tetrakis(4-(pyridin-4-yl)phenyl)ethene (TPPE) ligand enables the retention of high-pressure-induced green fluorescence at ambient conditions. Upon compression, structural contraction and conformational rearrangement of TPPE enhance π-conjugation, leading to a remarkable 140 nm pressure-induced fluorescence red-shift from cyan blue (452 nm) to yellow-green (592 nm), accompanied by a transition in emission intensity from strong to nearly quenched. Single-crystal X-ray diffraction (SCXRD) analysis further confirmed that the conformational change arose from variations in the torsion angles of the phenyl and pyridyl rings of TPPE, resulting in diminished molecular symmetry. This work establishes an effective strategy to "harvest" high-pressure emission states through conformational locking, offering guidance for the rational development of luminescent materials with tunable photophysical properties.

Introduction

Metal–organic frameworks (MOFs) are a class of porous crystalline materials constructed through the self-assembly of organic ligands with inorganic metal ions or clusters, which have garnered considerable attention owing to their tunable pore sizes, facile functionalization, and structural diversity.[1] Continued advances in MOF research have led to the development of the third generation, flexible MOFs (FMOFs), characterized by pore sizes that adapt responsively to external stimuli.[2,3] Susumu Kitagawa further classified FMOFs as soft porous crystals (SPCs), defined as porous solids possessing highly ordered networks and remarkable structural transformability.[4,5] In contrast to rigid inorganic porous materials, FMOFs rely on weak interactions—hydrogen bonding, coordination bonds, and π–π stacking—that impart structural flexibility to their frameworks.[6,7] Consequently, FMOFs undergo reversible structural transformations in response to diverse physical and chemical stimuli, including temperature, pressure, guest molecules, and light.[8] The unique stimulus–response dynamics confer exceptional versatility for the wide applications of FMOFs.[9,10] However, these materials usually experience structural collapse or loss of crystallinity upon external stimuli, and the resulting structural disorder greatly complicates their characterization.[11] As a result, the microscopic response mechanisms of FMOFs remain elusive, hindering the rational design and precise synthesis of function-oriented frameworks.

Tetraphenylethylene (TPE) represents one of the most prototypical aggregation-induced emission (AIE) luminogens.[12,13] Its ethylene core is surrounded by four freely rotatable phenyl rings, forming a propeller-like TPE molecule with a highly twisted conformation.[14] In solution, isolated TPE molecules are nearly non-emissive; conversely, they exhibit strong photoluminescence (PL) in the aggregated or the solid state, where the restriction of intramolecular rotation (RIR) effectively suppresses non-radiative decay.[15] The distinctive molecular flexibility of TPE and its derivatives (TPEs) enable reversible fluorescence color changes in response to external stimuli, driven by conformational rearrangements arising from aromatic ring rotations or phase transitions.[16–18] Recent studies have demonstrated that rational molecular design of AIE-based

[a]School of Resources, Environment and Materials, Guangxi University, Nanning 530004, China. E-mail: liaocz29@connect.hku.hk

[b]Engineering Research Center of Biomass Conversion and Biomass Oligosaccharides Engineering Technology Research Center of Anhui Province, Fuyang Normal University, Fuyang 236037, China. E-mail: ziyou.zhang@fynu.edu.cn

[c]Center for High Pressure Science and Technology Advanced Research, Shanghai, 201203, China. E-mail: zhiqiang.chen@hpstar.ac.cn

systems can effectively endow materials with diverse stimuli-responsive luminescence behaviors for applications such as information encryption and anti-counterfeiting.[19–22] Incorporating AIE luminogens into FMOFs not only restricts the rotation of phenyl rings through coordination bonds to achieve efficient luminescence but also imparts the framework with unique flexibility under external stimuli.[23,24] Such integration provides an ideal platform for exploring the interrelationship between structure and photophysical properties of FMOFs under pressure.

Pressure, as a crucial thermodynamic parameter, enables the regulation of macroscopic properties by altering microstructures and bonding configurations without changing the material's chemical composition.[25–28] Su *et al.* reported that a flexible MOF retained redshifted fluorescence upon compression, as the coordination locking facilitated weak π–π interactions between adjacent AIE ligands, which intensified rapidly with increasing pressure.[29] Similarly, Zou *et al.* realized pressure-induced PL emission enhancement in $Tb(BTC)(H_2O)_6$ *via* pressure engineering, in which strengthened hydrogen bonds locked the conjugated configuration formed by the carboxyl group and benzene ring of the organic ligands.[30] However, high-pressure phases that persist at ambient conditions after compression–decompression treatment are rarely reported, rendering the pressure–structure–property correlation unclear.

Herein, we conclusively realized piezochromic behaviors in a three-dimensional MOF, $[Cd_2(\text{D-Cam})_2(\text{TPPE})]_n$ (D-MOF), assembled from the flexible AIEgen TPPE and the chiral D-(+)-camphoric acid (D-H_2Cam). Upon compression, the intermolecular distance between TPPE ligands decreases, promoting the formation of π–π stacked excimers that triggered a pronounced 140 nm redshift (from 452 nm at ambient pressure to 592 nm at 10.1 GPa), accompanied by a color evolution from cyan-blue to blue-green, green, and yellow-green. After decompression, the D-MOF remarkably retained the green luminescent state of the high-pressure phase. *In situ* high-pressure Raman and infrared (IR) spectra demonstrated that the microscopic crystal structure remained intact throughout the compression–decompression process, with the framework preserved. Notably, the decompressed single crystal maintained the high-pressure phase, undergoing a structural transition from space group $P6_222$ to $P3_221$. Density functional theory (DFT) calculations revealed that pressure-induced torsion of the phenyl and pyridyl rings expanded the π-conjugated system of TPPE. This work uniquely captured a high-pressure phase of the D-MOF at ambient conditions through ligand-conformation locking, clearly elucidating the relationship between pressure, structure, and fluorescence properties, and offering novel insights for rationally tuning the photophysical behaviors of functional materials.

Results and discussion

The AIEgen-based optically pure D-MOF single crystal was successfully synthesized *via* a solvothermal method following the previously reported procedure[31](detailed procedures are provided in the SI). The experimental powder X-ray diffraction pattern agrees well with the simulated pattern generated from the single-crystal structure (Fig. S1). The D-MOF crystallizes in the chiral hexagonal system with the $P6_222$ space group, consistent with that of natural β-quartz. Each Cd^{2+} ion is six-coordinated, coordinating with two TPPE molecules and two D-H_2Cam molecules. The carboxyl groups of D-H_2Cam chelate in a bidentate fashion, whereas the pyridyl nitrogens of TPPE coordinate monodentately.[31] The D-Cam molecules impart their chirality to the achiral TPPE molecules mediated by Cd^{2+} ions *via* the through-space chirality transfer (TSCT). Consequently, the three building blocks—Cd^{2+} ion polyhedra, D-Cam, and TPPE—collectively adopt a right-handed three-dimensional packing arrangement (Fig. 1a).

Under ambient conditions, the D-MOF emits an intense cyan-blue fluorescence upon excitation at 365 nm, with an emission maximum at 452 nm.[31] The emission mechanism is attributed to framework enabled emission (FEE), where the vibrations and partial rotations of TPPE molecules are restricted by coordination, despite their spatially discrete distribution in the D-MOF crystal.[31] The fluorescence behavior of TPE luminophores is intrinsically governed by intramolecular motion and intermolecular stacking states. Rotations of phenyl rings and variations in dihedral angles allow them to respond to external stimuli, ultimately manifesting as alterations in photophysical properties.[32] Meanwhile, D-H_2Cam, as a flexible alkane molecule, can be compressed upon external force, which modulates molecular packing and thereby affects the overall macroscopic behavior.[33] Therefore, integrating TPPE and D-H_2Cam within a single framework imparts the D-MOF with exceptional structural flexibility and outstanding optical responsiveness toward mechanical stimuli such as grinding and ultrasonication.[31]

In light of these findings, we further investigated the luminescent behavior of the D-MOF under high pressure. To this end, a diamond anvil cell (DAC) capable of generating precisely controlled hydrostatic pressure was employed for a series of *in situ* high-pressure experiments. Fig. 1b and S2 presents the *in situ* PL spectra of the D-MOF under compression. The fluorescence intensity gradually declined as the pressure increased to 10.1 GPa, and upon further compression to higher pressures, the emission signal became nearly quenched. It is noticeable that the emission wavelength underwent a redshift of approximately 140 nm, from 452 nm to 592 nm, with the observed color changes from cyan-blue to blue-green, green, and yellow-green (Fig. 1c and d). Of particular interest, throughout the compression process, both the fluorescence intensity and peak position initially varied rapidly at lower pressures and then evolved more slowly under further compression (Fig. 1e). During gradual pressure release, the fluorescence emission reemerged with progressively increasing intensity (Fig. 1c, S3 and S4). Remarkably, at full decompression, the emission peak shifted back to 515 nm (cyan-green), substantially redshifted relative to the original 452 nm, with a broadened peak profile, indicating that the D-MOF experienced partially irreversible structural changes (Fig. 1f and S5). Additionally, fluorescence spectra were collected during three consecutive compression–decompression cycles (Fig. S6 and S7). Notably, the emission was eventually quenched around 600 nm, although higher

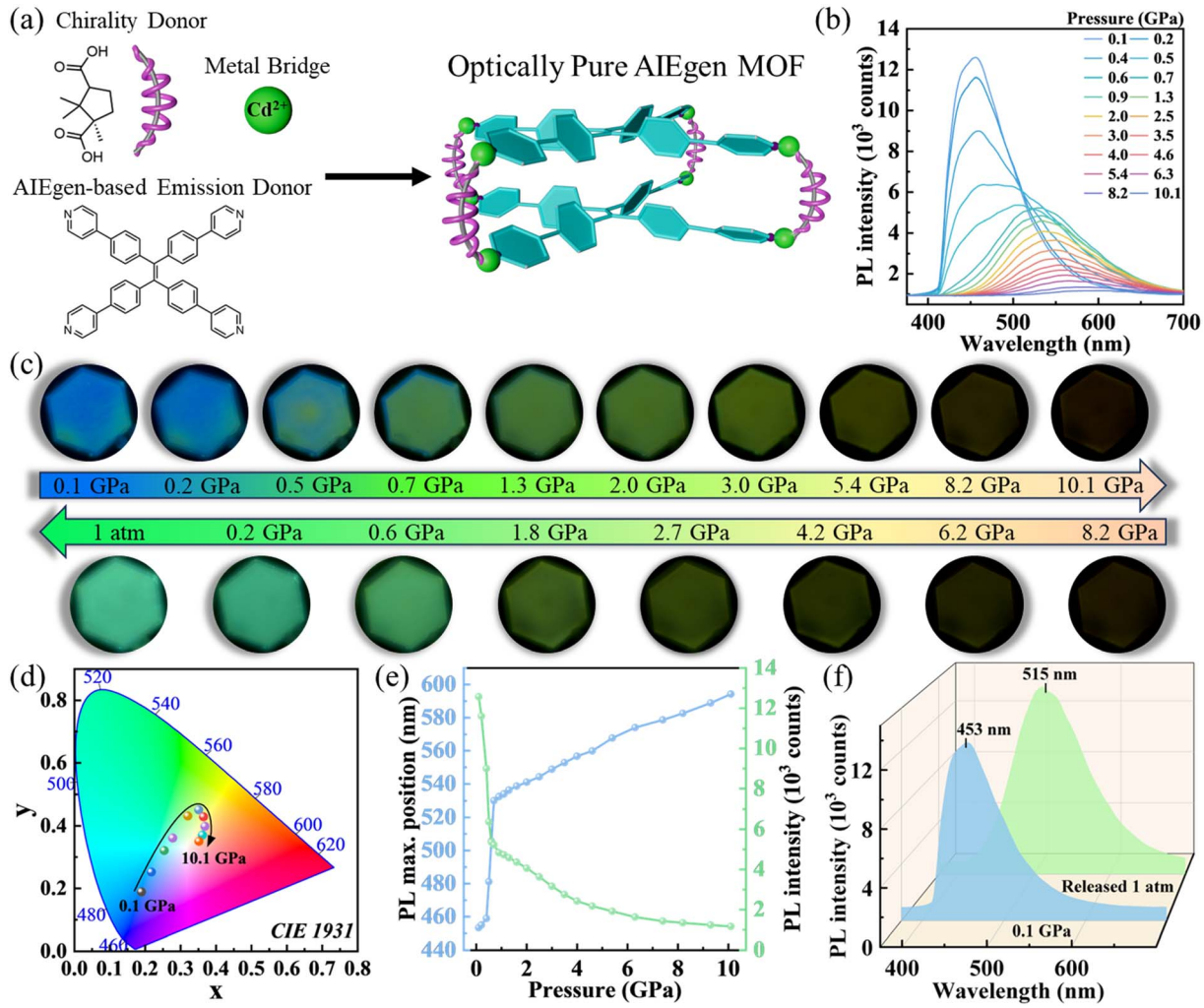

Fig. 1 (a) Schematic illustration of the chiral reticular self-assembly strategy of the D-MOF. (b) *In situ* high-pressure PL spectra of the D-MOF during compression. (c) PL micrographs of the D-MOF during compression and decompression. (d) CIE chromaticity diagram of the D-MOF during compression. (e) Pressure-dependent evolution of PL intensity and emission wavelength of the D-MOF up to 10.1 GPa. (f) Comparison of the PL spectra of the D-MOF at 0.1 GPa and after complete pressure release from 10.1 GPa.

pressures were required in subsequent cycles. After complete pressure release, the emission wavelengths gradually converged. This implies that pressure treatment probably drives the D-MOF into a lower-energy equilibrium state that is stably maintained after decompression, thereby giving rise to a luminescence "memory effect". Temperature-dependent PL spectra were also recorded (Fig. S8). The emission intensity gradually decreases and the emission peak broadens with increasing temperature. Upon cooling, the emission peak position nearly returns to its initial state, indicating that the luminescence response of the D-MOF is specific to pressure stimulation.

To further probe the PL decay kinetics of the D-MOF, *in situ* high-pressure time-resolved PL (TRPL) spectra were recorded (Fig. S9 and S10). The decay curves were fitted using a double exponential function,[34] yielding the variation of the average PL lifetime as a function of pressure (Table S1 and Fig. 2a). Upon compression, the average lifetime decreased continuously from 1.78 ns at ambient conditions to 0.67 ns at 9.2 GPa, consistent with the observed decline in PL intensity. The continuous reduction in the PL lifetime of the D-MOF was primarily attributed to pressure-induced framework contraction, which enhanced intermolecular interactions and thus introduced additional non-radiative decay channels.[32] After decompression, the average fluorescence lifetime increased, reaching 2.96 ns at ambient conditions, prominently longer than the initial value of 1.78 ns (Fig. 2b and c). Because the decay kinetics of solid-state luminophores are largely determined by molecular dynamics (vibrations and rotations), the elongated lifetime implies that the conformational motions in the D-MOF are more effectively restricted.[35]

To elucidate the fluorescence evolution mechanism at the molecular level, *in situ* high-pressure UV-vis absorption, IR and Raman spectroscopies were conducted. As shown in Fig. 2d, the D-MOF displays a pronounced absorption peak at 380 nm, attributed to the π–π* local electron transition of TPPE molecules.[36] With increasing pressure up to 10.5 GPa, the absorption

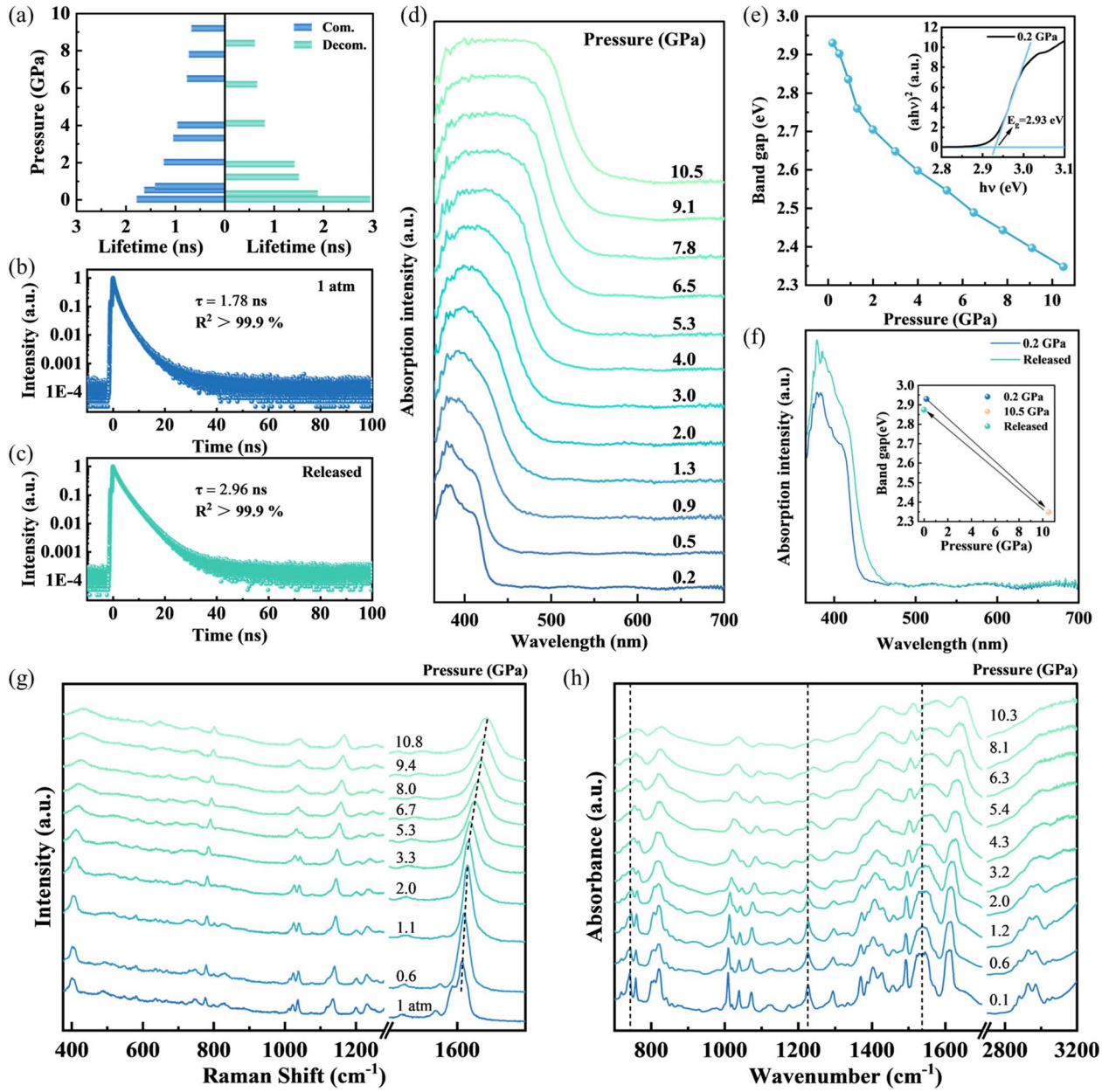

Fig. 2 (a) Pressure-dependent variation of the average PL lifetime of the D-MOF. Normalized time-resolved PL decay curves of the D-MOF (b) before compression and (c) released. (d) *In situ* high-pressure UV-vis absorption spectra of the D-MOF during compression. (e) Evolution of the optical band gap of the D-MOF as a function of pressure, with the inset showing the Tauc plot at 0.2 GPa. (f) Comparison of UV-vis absorption spectra at 0.2 GPa and after pressure treatment, with the inset illustrating the corresponding band gap change. *In situ* high-pressure (g) Raman spectra and (h) IR spectra of the D-MOF upon compression.

peak underwent a continuous redshift, accompanied by peak broadening and enhanced intensity. The pressure-dependent band gap of the D-MOF was determined using the direct band gap Tauc plots,[37] where $(\alpha h\nu)^2$ is plotted against $h\nu$ (Fig. 2e). Upon compression from 0.2 to 10.5 GPa, the band gap progressively decreased from 2.93 eV to 2.35 eV. These results suggest that pressure strengthens intermolecular interactions and induces conformational changes in TPPE, which enhance molecular conjugation. Therefore, the energy gap of the π–π* transition decreases, resulting in redshifted absorption and a progressive reduction in the band gap.[38] After decompression, the UV-vis absorption spectrum did not thoroughly revert to its original peak positions, and the band gap remained 0.06 eV lower than the initial value (Fig. 2f, S11 and S12). This incomplete recovery indicates that the D-MOF did not fully restore its original electronic structure, accounting for the redshift in fluorescence emission.

The *in situ* high-pressure Raman spectra of the D-MOF are shown in Fig. 2g. The Raman peak at 1036 cm^{-1} corresponds to the in-plane bending vibration of the pyridine ring,[39] the peak at

1135 cm^{-1} arises from the stretching vibration of the C–C single bond formed between the ethylene core and the adjacent benzene ring in TPPE, and the peak at 1607 cm^{-1} is attributed to the C=C stretching vibration of the benzene ring.[40] With increasing pressure, all Raman peaks exhibit a distinct blueshift, peak broadening, and reduced intensities, collectively indicating the escalated intermolecular interactions. Upon decompression, most Raman peaks almost recover to their initial positions (Fig. S13 and S14). Notably, the Raman peak at 1607 cm^{-1} displays a pressure-dependent shift with two distinct regimes. In the low-pressure region (<1.1 GPa), this peak shows a relatively rapid blueshift. As the pressure further increases, the shift rate becomes noticeably slower, which may be associated with the conformational planarization of the TPPE ligand.[36] Throughout the entire compression–decompression cycle, no new Raman peaks emerged nor did any vanish. Combined with the *in situ* PL and UV-vis results, these observations manifest that the D-MOF undergoes an isostructural phase transition.

The *in situ* high-pressure IR spectra showed trends consistent with the Raman results (Fig. 2h). The IR bands in the range of 700–900 cm^{-1} are attributed to the C–H deformation vibrations (δ(C–H)).[41] The peak located at 1293 cm^{-1} is assigned to the C–N stretching vibration (ν(C–N)).[42] In addition, the band at 1535 cm^{-1} is attributed to the C=C stretching vibration (ν(C=C)) of the benzene ring skeleton.[43] The broad absorption band centered at 2950 cm^{-1} can be assigned to the C–H stretching vibration (ν(C–H)).[44] As pressure increases, all IR peaks shifted toward higher wavenumbers, implying the compressed framework, shortened bond lengths, and consequently enhanced vibrational frequencies. Moreover, distinct vibrational modes exhibited different pressure responses.[45] Below 1.2 GPa, the response was governed by framework contraction, producing a profound blueshift of the IR peaks above 1500 cm^{-1}. At higher pressures, conformational rearrangements became predominant, leading to more noticeable blueshifts in the low-wavenumber region. Meanwhile, changes in the profiles of most IR peaks revealed stronger intermolecular interaction under compression.[44] These spectral features reasonably accounted for the rapid variations in the PL emission peak position and intensity at low pressure, as well as the more gradual evolutions observed under higher pressure. Upon pressure release, most IR peaks returned near their original positions (Fig. S15 and S16).

The *in situ* high-pressure PL measurements revealed that upon full decompression, the D-MOF retained a fluorescence peak at 515 nm, redshifted by 63 nm compared to its initial emission. This clearly evidences that the high-pressure phase was successfully preserved under ambient conditions. Single-crystal X-ray diffraction (SCXRD) was carried out on the completely decompressed sample and further confirmed that the crystal structure was successfully resolved, capturing the metastable phase retained after the high-pressure-induced conformational transition. The crystallographic parameters of the D-MOF before and after compression are summarized in Table S2, and the selected bond lengths and bond angles of the released D-MOF are listed in Table S3. Upon complete decompression, the *a*-axis and *b*-axis slightly elongated by ~0.1 Å, while the *c*-axis decreased from 47.860 Å to 47.635 Å, ultimately resulting in an enlarged unit cell volume. And the space group changed from $P6_222$ to $P3_221$, revealing a conformation-driven phase transition induced by pressure. To further elucidate the origin of the reduced symmetry, the conformational evolution of the flexible TPPE ligand within the D-MOF was comparatively analyzed. Relative to the conformation at ambient conditions, TPPE ligands exhibited substantial conformational changes after pressure treatment (Fig. 3a and Table S4). Specifically, the average dihedral angle P1–P2 decreased from 56.16° to 55.99°, while the average dihedral angle P2–P3 decreased from 27.64° to 26.06°. The four symmetrically distributed pyridyl-phenyl units transformed into a pairwise symmetrical arrangement. This conformational evolution expanded the π-conjugation of TPPE and enhanced electron delocalization, thereby modulating the energy level structure of the emission and ultimately resulting in a marked redshift of fluorescence. Further comparison of the layered structures of the D-MOF before and after compression (Fig. 3b and c) showed reductions in TPPE interlayer spacing and D-H_2Cam interlayer spacing by 7 pm and 4 pm, respectively. This demonstrated that the overall layered feature of the framework nearly recovered to its initial state upon full pressure release, confirming that the PL redshift primarily originated from the conformational rearrangement of TPPE molecules. For comparison, previous studies on AIE-based MOFs generally reported reversible luminescence responses under pressure. For example, Zhang *et al.* observed reversible fluorescence evolution in an AIE-Mn-MOF,[29] while Guo *et al.* reported reversible pressure-responsive luminescence in TPE-based Sr-ETTB attributed to the intrinsic flexibility of the framework.[40] In contrast, the D-MOF partially retains the high-pressure luminescent state after decompression, indicating that pressure-induced conformational changes of the TPPE ligand can be stabilized by framework confinement, resulting in a ligand conformational locking effect. To the best of our knowledge, no prior work has been reported about this successful retention of a metastable phase induced by pressure-driven conformational transition in a flexible MOF. This finding not only clearly provides insight into the intrinsic relationship between pressure-driven structural transformation and structure–property modulation, but also validates the feasibility flexible-ligand conformational-locking strategy for capturing high-pressure emissive states.[46,47]

To quantitatively clarify how the conformational changes of the flexible TPPE ligands in the D-MOF influence its optical properties, we calculated the HOMO–LUMO energy gap of TPPE before and after compression (Fig. 4a). It was revealed that both HOMO and LUMO levels shifted toward the vacuum level after compression, indicating enhanced electron delocalization. Concurrently, the slightly reduced energy gap suggested that TPPE conformational rearrangement promoted π-electron delocalization throughout the molecular framework, thereby expanding the conjugated system and underpinning the PL redshift of the D-MOF after pressure treatment. According to Kasha's rule,[48] molecular fluorescence typically originates from the first singlet excited state (S_1). Therefore, electron–hole

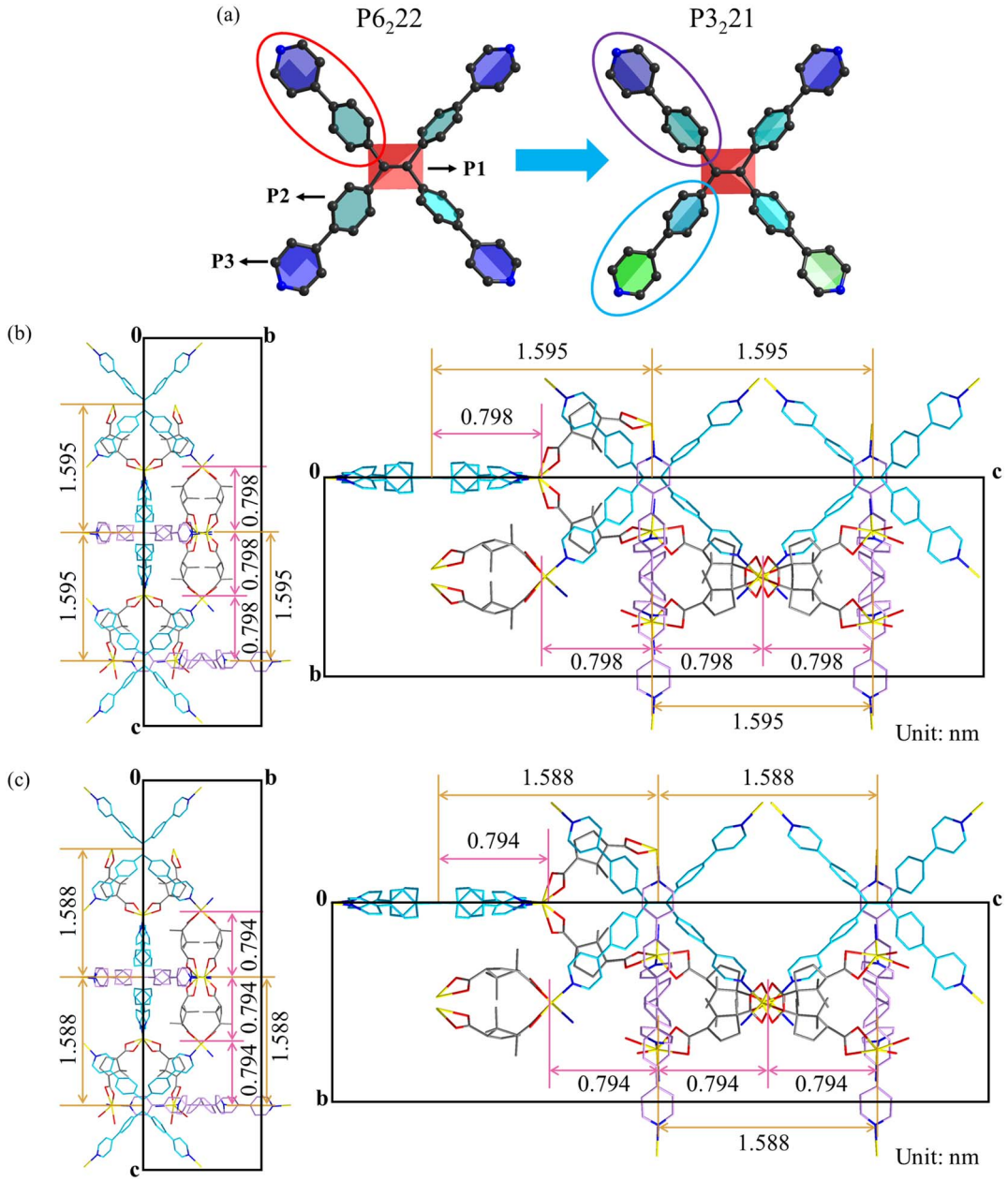

Fig. 3 (a) Conformational changes of the TPPE ligand in the D-MOF before and after compression (Plane P1 is defined by the two C atoms forming the central C=C double bond and four C atoms surrounding them. The phenyl rings and pyridine ring define the P2 and P3 planes crossing them, respectively). (b) (c) Comparison of the layered characteristics in the D-MOF single-crystal: (b) original and (c) released states.

analysis was performed to elucidate the electronic transition characteristics associated with the $S_0 \rightarrow S_1$ excitation of the TPPE ligand in the D-MOF. As shown in Fig. S17, under ambient conditions both electrons and holes are mainly distributed over the π-conjugated framework of the TPPE. After pressure treatment, their spatial distributions exhibit an approximately pairwise symmetric pattern. Table 1 summarizes the electron–hole distribution parameters of TPPE in the $S_0 \rightarrow S_1$ excited state. The centroid distance between the mass centers of electrons and holes (D) decreases from 14.365 Å to 9.233 Å, while the degree of separation (t) decreases from 8.982 Å to 6.898 Å, indicating a reduced spatial separation of the excited carriers. In addition, the hole delocalization index (HDI) and electron delocalization index (EDI) increase by 0.25 and 0.39, respectively, suggesting enhanced delocalization of both electrons and holes over the π-conjugated framework. Furthermore, analysis of the molecular electrostatic potential (MEP, Fig. 4b) manifested that prior to compression, high electron-density regions (red region) were concentrated near the four pyridyl nitrogen atoms, whereas the ethylene core and phenyl rings primarily exhibited a positive potential (blue region). After decompression, the electron-rich regions around nitrogen atoms diminished, while the positive potential regions expanded, suggesting reduced molecular polarization and a redistribution of electron

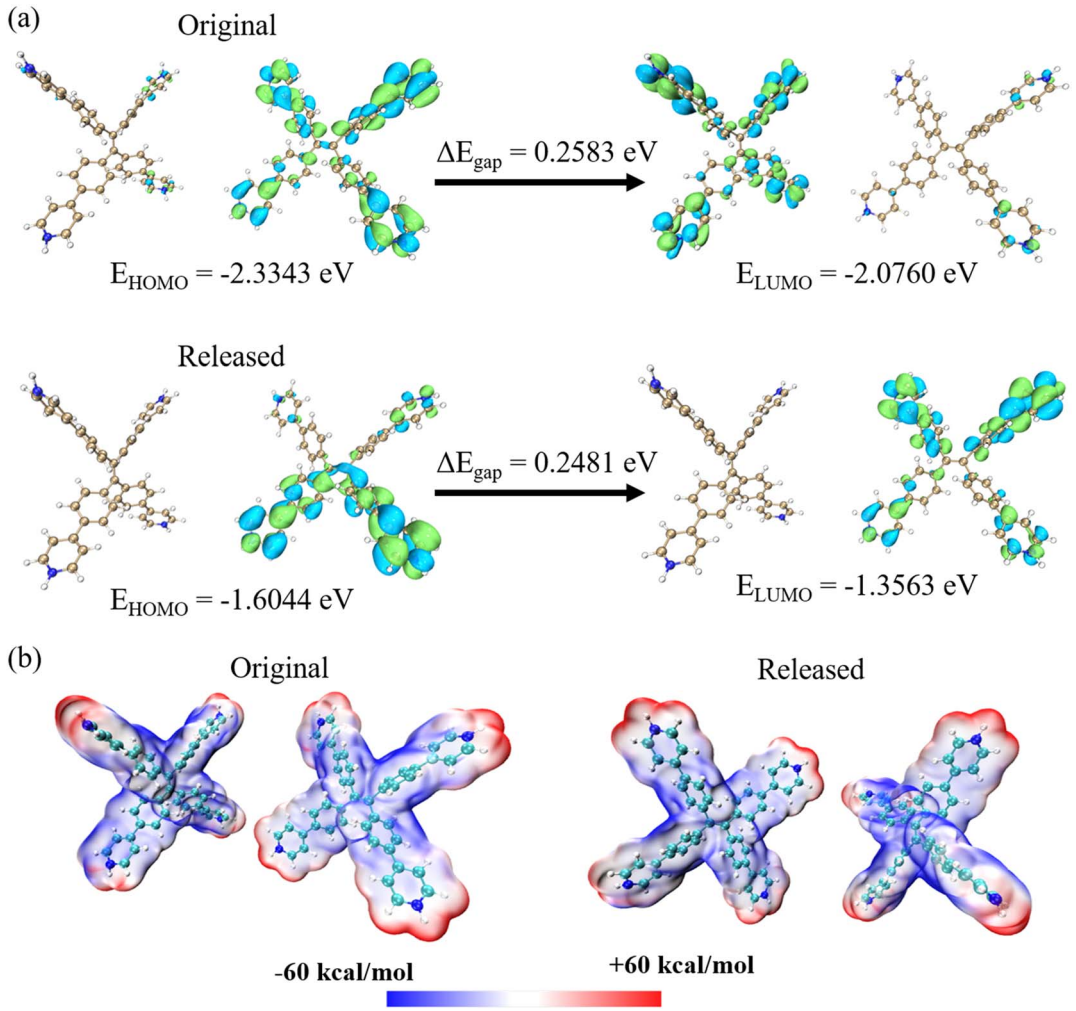

Fig. 4 (a) Contour plots of the HOMO, LUMO, and HOMO–LUMO energy gap of the TPPE ligand in the D-MOF before and after compression. (b) Molecular electrostatic potential of the TPPE ligand in the D-MOF before and after compression.

Table 1 Parameters of hole and electron distributions of the TPPE in the D-MOF under the excited state of $S_0 \rightarrow S_1$[a]

	Original	Released
D (Å)	14.365	9.233
Sr	0.54268	0.24722
H (Å)	8.479	5.447
t (Å)	8.982	6.898
HDI	4.21	6.26
EDI	4.46	6.65

[a] *D* is the delocalization index, Sr is the integral of geometric mean function of holes and electrons, *H* is the overall average distribution breadth of electrons and holes, *t* is the degree of separation between holes and electrons, HDI is the hole delocalization index, and EDI is the electron delocalization index.

density toward more uniform delocalization across the π-framework. Such electron density redistribution was consistent with the narrowed HOMO–LUMO gap, thereby providing further evidence from the electronic-structure perspective for the pressure-modulated optical properties of the D-MOF.

Conclusions

In summary, we systematically investigated the fluorescence response behavior and conformational regulation mechanism of the TPPE-based chiral luminescent MOF (D-MOF) under high-pressure conditions. By leveraging the high conformational sensitivity of flexible organic ligands to pressure, a broad pressure-induced fluorescence shift from cyan-blue (452 nm) to yellow-green (592 nm) was realized. Notably, we presented a previously unexplored approach in which the high-pressure phase of the flexible MOF has been successfully retained under ambient conditions. By integrating a series of *in situ* high-pressure spectroscopic techniques, we revealed the entire process of enhanced π-conjugation driven by pressure-induced conformational rearrangements of the TPPE ligand. SCXRD analysis further confirmed that changes in the torsional angles of TPPE phenyl and pyridyl rings reduced molecular symmetry, which underlies the irreversible PL redshift. Moreover, the D-MOF demonstrated robust structural stability and a PL "memory effect" during repeated pressure cycles, endowing it

with outstanding tunability in luminescence. Overall, this work establishes a strategy for capturing high-pressure luminescent states through conformational locking of flexible AIE ligands, offering new insights for the design of stimulus-responsive luminescent materials.

Author contributions

Y. Fan performed the *in situ* high-pressure experiments, data analysis and manuscript writing. Z. Y. Zhang prepared the sample, performed theoretical calculations, carried out single-crystal X-ray analyses, and developed the idea for the study. Z. K. Zhu, S. Zhou, F. Gorelli, Y. C. Ye, H. X. Hu, S. H. Zhang, and H. L. Dong assisted with the data collection and analyses. C. Z. Liao, Z. Y. Zhang, and Z. Q. Chen contributed to the writing and revisions of the manuscript.

Conflicts of interest

There are no conflicts to declare.

Data availability

CCDC 2514434 contains the supplementary crystallographic data for this paper.[49]

The data supporting this article have been included as part of the supplementary information (SI). Supplementary information: experimental details, *in situ* high-pressure PL spectra, TRPL spectra, UV-vis absorption spectra, Raman spectra, IR spectra and crystallographic data. See DOI: https://doi.org/10.1039/d5sc09651k.

Acknowledgements

This work was financially supported by NSAF (Grant No. U1530402), China. SCXRD measurement was performed at beamline BL17B of the National Facility for Protein Science in Shanghai (NFPS), Shanghai Advanced Research Institute, CAS. The authors thank Drs Gang Liu and Lingping Kong from the Center for High Pressure Science and Technology Advanced Research (HPSTAR) for their valuable assistance with data collection.

Notes and references

1 N. Kajal, V. Singh, R. Gupta and S. Gautam, *Environ. Res.*, 2022, **204**, 112320.
2 K. B. Thapa, S. Lee and S. Park, *Mater. Today Adv.*, 2025, **26**, 100588.
3 T. Kundu, M. Wahiduzzaman, B. B. Shah, G. Maurin and D. Zhao, *Angew. Chem., Int. Ed.*, 2019, **58**, 8073–8077.
4 S. Kitagawa and M. Kondo, *Bull. Chem. Soc. Jpn.*, 1998, **71**, 1739–1753.
5 S. Horike, S. Shimomura and S. Kitagawa, *Nat. Chem.*, 2009, **1**, 695–704.
6 J. H. Lee, S. Jeoung, Y. G. Chung and H. R. Moon, *Coord. Chem. Rev.*, 2019, **389**, 161–188.
7 Y. Li, Y. Wang, W. Fan and D. Sun, *Dalton Trans.*, 2022, **51**, 4608–4618.
8 N. Li, J. Pang, F. Lang and X. Bu, *Acc. Chem. Res.*, 2024, **57**, 2279–2292.
9 A. Schneemann, V. Bon, I. Schwedler, I. Senkovska, S. Kaskel and R. A. Fischer, *Chem. Soc. Rev.*, 2014, **43**, 6062–6096.
10 I. Senkovska, V. Bon, A. Mosberger, Y. Wang and S. Kaskel, *Adv. Mater.*, 2025, **37**, 2414724.
11 R. Pallach, J. Keupp, K. Terlinden, L. Frentzel-Beyme, M. Kloß, A. Machalica, J. Kotschy, S. K. Vasa, P. A. Chater, C. Sternemann, M. T. Wharmby, R. Linser, R. Schmid and S. Henke, *Nat. Commun.*, 2021, **12**, 4097.
12 Y. Hong, J. W. Y. Lam and B. Z. Tang, *Chem. Commun.*, 2009, 4332–4353.
13 J. Mei, N. L. C. Leung, R. T. K. Kwok, J. W. Y. Lam and B. Z. Tang, *Chem. Rev.*, 2015, **115**, 11718–11940.
14 V. Kachwal and I. R. Laskar, *Top. Curr. Chem.*, 2021, **379**, 28.
15 D. D. La, S. V. Bhosale, L. A. Jones and S. V. Bhosale, *ACS Appl. Mater. Interfaces*, 2018, **10**, 12189–12216.
16 G. Huang, X. Du, H. Bo and B. S. Li, *Mater. Chem. Front.*, 2024, **8**, 104–132.
17 Z. An, Z. Dai, J. Liu, S. Chen, X. Wang, H. Liu, Z. Sheng and T. Shan, *Adv. Sci.*, 2024, **11**, 2409974.
18 Z. Yang, Z. Chi, Z. Mao, Y. Zhang, S. Liu, J. Zhao, M. P. Aldred and Z. Chi, *Mater. Chem. Front.*, 2018, **2**, 861–890.
19 W. Zhong, J. Zhang, Y. Lin, S. Li, Y. Yang, W. Wang, C. Si, F. E. Kühn, Z. Zhao, X. Cai and B. Z. Tang, *Chem. Sci.*, 2024, **15**, 3920–3927.
20 X. Chen, C. Cheng, Y. Yu, W. Zhong, Z. Zhao, S. Yang, Z. Zhao, J. Zhang and X. Cai, *Chem. Commun.*, 2025, **61**, 19632–19635.
21 Y. Wu, Z. Xin, Y. Lin, S. Yang, Z. Zhao, W. Wang, B. Z. Tang and X. Cai, *Adv. Funct. Mater.*, 2026, **36**, e8618.
22 D. Wang, X. Chen, Y. Lin, L. Wu, Z. Zhao, X. Xu, S. Yang, J. Zhang, W. Wang, Z. Zhao, S. Wang, B. Z. Tang and X. Cai, *Chem. Sci.*, 2026, **17**, 2847–2857.
23 N. B. Shustova, B. D. McCarthy and M. Dincă, *J. Am. Chem. Soc.*, 2011, **133**, 20126–20129.
24 Z. Wei, Z. Gu, R. K. Arvapally, Y. Chen, R. N. McDougald Jr, J. F. Ivy, A. A. Yakovenko, D. Feng, M. A. Omary and H. Zhou, *J. Am. Chem. Soc.*, 2014, **136**, 8269–8276.
25 Y. C. Shang, Z. D. Liu, J. J. Dong, M. G. Yao, Z. X. Yang, Q. J. Li, C. G. Zhai, F. R. Shen, X. Y. Hou, L. Wang, N. Q. Zhang, W. Zhang, R. Fu, J. F. Ji, X. M. Zhang, H. Lin, Y. W. Fei, B. Sundqvist, W. H. Wang and B. B. Liu, *Nature*, 2021, **599**, 599–604.
26 A. P. Drozdov, M. I. Eremets, I. A. Troyan, V. Ksenofontov and S. I. Shylin, *Nature*, 2015, **525**, 73–76.
27 Y. M. Ma, M. Eremets, A. R. Oganov, Y. Xie, I. Trojan, S. Medvedev, A. O. Lyakhov, M. Valle and V. Prakapenka, *Nature*, 2009, **458**, 182–185.
28 J. Gong, H. Zhong, C. Gao, J. Peng, X. Liu, Q. Lin, G. Fang, S. Yuan, Z. Zhang and X. Xiao, *Adv. Sci.*, 2022, **9**, 2201554.
29 Z. Zhang, T. Ji, H. Dong, Z. Chen and Z. Su, *Chin. Chem. Lett.*, 2024, **35**, 109542.

30 Y. Wang, X. Yang, C. Liu, Z. Liu, Q. Fang, F. Bai, S. Wang, X. Hou, B. Feng, B. Chen and B. Zou, *Angew. Chem., Int. Ed.*, 2022, **61**, e202210836.
31 W. Shang, X. Zhu, T. Liang, C. Du, L. Hu, T. Li and M. Liu, *Angew. Chem., Int. Ed.*, 2020, **59**, 12811–12816.
32 H. Yuan, K. Wang, K. Yang, B. Liu and B. Zou, *J. Phys. Chem. Lett.*, 2014, **5**, 2968–2973.
33 Z. Zhang, D. Deng, X. Xu, J. Zhang, S. Yan, Z. Guo, H. Dong, Z. Chen and Z. Su, *JACS Au*, 2024, **4**, 2050–2057.
34 D. Shi, V. Adinolfi, R. Comin, M. Yuan, E. Alarousu, A. Buin, Y. Chen, S. Hoogland, A. Rothenberger, K. Katsiev, Y. Losovyj, X. Zhang, P. A. Dowben, O. F. Mohammed, E. H. Sargent and O. M. Bakr, *Science*, 2015, **347**, 519–522.
35 E. Ramachandran and R. Dhamodharan, *J. Mater. Chem. C*, 2017, **5**, 10469–10476.
36 J. Wu, J. Tang, H. Wang, Q. Qi, X. Fang, Y. Liu, S. Xu, S. X. Zhang, H. Zhang and W. Xu, *J. Phys. Chem. A*, 2015, **119**, 9218–9224.
37 J. Tauc, R. Grigorovici and A. Vancu, *Phys. Status Solidi B*, 1966, **15**, 627–637.
38 A. Li, Z. Ma, J. Wu, P. Li, H. Wang, Y. Geng, S. Xu, B. Yang, H. Zhang, H. Cui and W. Xu, *Adv. Opt. Mater.*, 2018, **6**, 1700647.
39 K. Traikov, Z. Dong, S. Xie, Y. Song, Z. Liu and K. K. Zhuravlev, *Phys. Rev. B:Condens. Matter Mater. Phys.*, 2010, **82**, 064116.
40 X. Guo, N. Zhu, S. P. Wang, G. Li, F. Q. Bai, Y. Li, Y. Han, B. Zou, X. B. Chen, Z. Shi and S. Feng, *Angew. Chem., Int. Ed.*, 2020, **59**, 19716–19721.
41 J. Fang, X. Yu, Y. Liu, Y. Yusran, Y. Wang, V. Valtchev, S. Qiu, B. Zou and Q. Fang, *Angew. Chem., Int. Ed.*, 2024, **63**, e202409099.
42 J. Fang, Z. Fu, X. Chen, Y. Liu, F. Chen, Y. Wang, H. Li, Y. Yusran, K. Wang, V. Valtchev, S. Qiu, B. Zou and Q. Fang, *Angew. Chem., Int. Ed.*, 2023, **62**, e202304234.
43 Y. Wang, Y. Yin, B. Yang, W. Tian, X. Yang and B. Zou, *Nano Lett.*, 2025, **25**, 2141–2149.
44 S. Tong, J. Dai, J. Sun, Y. Liu, X. Ma, Z. Liu, T. Ma, J. Tan, Z. Yao, S. Wang, H. Zheng, K. Wang, F. Hong, X. Yu, C. Gao and X. Gu, *Nat. Commun.*, 2022, **13**, 5234.
45 S. Li, Q. Wang, Y. Qian, S. Wang, Y. Li and G. Yang, *J. Phys. Chem. A*, 2007, **111**, 11793–11800.
46 N. B. Shustova, A. F. Cozzolino and M. Dincă, *J. Am. Chem. Soc.*, 2012, **134**, 19596–19599.
47 Z. Xiong, Y. Li, J. Liang, S. Xiang, Y. Lv and Z. Zhang, *ACS Appl. Mater. Interfaces*, 2022, **14**, 38098–38104.
48 M. Kasha, *Discuss. Faraday Soc.*, 1950, **9**, 14–19.
49 CCDC 2514434: Experimental Crystal Structure Determination, 2026, DOI: 10.5517/ccdc.csd.cc2qdgsd.